The potential of drone observations to improve air quality predictions by 4D-var

Hassnae Erraji[1], Philipp Franke[1], Astrid Lampert[2], Tobias Schuldt[1], Ralf Tillmann[1], Andreas Wahner[1], and Anne Caroline Lange[1]

[1]Forschungszentrum Jülich GmbH, Institute of Energy and Climate Research - Troposphere (IEK-8), Jülich, Germany
[2]Institute of Flight Guidance, TU Braunschweig, Braunschweig, Germany

Correspondence: A. C. Lange (ann.lange@fz-juelich.de)

Abstract. Vertical profiles of atmospheric pollutants, acquired by unmanned aerial vehicles (UAVs, known as drones), represent a new type of observation that can help to fill the existing observation gap in the planetary boundary layer. In this article, the first study of assimilating air pollutant observations from drones is presented to evaluate the impact on local air quality analysis. The study uses the high-resolution air quality model EURAD-IM (EURopean Air pollution Dispersion – Inverse Model), including the four-dimensional variational data assimilation system (4D-var), to perform the assimilation of ozone (O_3) and nitrogen oxide (NO) vertical profiles. 4D-var takes advantage of the inverse technique and allows for simultaneous adjustments of initial values and emissions rates. The drone data was collected during the MesSBAR (Automatisierte luftgestützte **Mes**sung der **S**chadstoff**B**elastung in der erdnahen **A**tmosphäre in urbanen **R**äumen / Automated airborne measurement of air pollution levels in the near earth atmosphere in urban areas) field campaign, which was conducted on 22-23 September 2021 in Wesseling, Germany. The two-day analyses reveal that the 4D-var assimilation of high-resolution drone measurements has a beneficial impact on the representation of regional air quality in the model. On both days, a significant improvement in the vertical distribution of O_3 and NO is noticed in the analysis compared to the reference simulation without data assimilation. Moreover, the validation against independent observations shows an overall improvement in the bias, root-mean-square error, and correlation for O_3, NO, and NO_2 (nitrogen dioxide) ground concentrations at the measurement site as well as in the surrounding region. Furthermore, the assimilation allows for the deduction of emission correction factors in the grid cells surrounding the measurement site, which significantly contribute to the observed improvement in the analysis.

1 Introduction

In response to the increasing need for high-resolution and accurate air-quality forecasts, extended efforts to improve the performance of chemical transport models (CTM) have been made over recent decades. One of the effective means of improvement involves the use of advanced data assimilation techniques (Elbern et al., 2007; Liu et al., 2017; Klonecki et al., 2012). The aim is to combine observations and model data to obtain a better representation of the pollutants in the atmosphere as well as to optimise the input parameters, such as emissions, when considering inverse models. Although data assimilation holds significant potential for enhancing air quality modelling, its application is often still limited due to the scarcity of available observational

data. In fact, the observational data types, which are usually used for assimilation (ground-based, airborne, and satellite observations), are certainly valuable for enhancing forecast accuracy, but they remain insufficient due to various constraints related to their availability, resolution, and especially their limited vertical coverage. Ground-based observations are the major source of information for regional CTMs and are generally taken from in-situ monitoring networks. Even if they are fairly dense in the horizontal distribution on a regional scale, no information regarding the vertical distribution of air pollutants is provided. In contrast, lidar (light detection and ranging) remote sensing instruments and in-situ sonde measurements can provide this information, but unfortunately, only a sparse and limited number of such stations exist. Similarly, airborne observations (e.g., IAGOS or flight campaigns) provide vertical profiles during take-off and landing; however, the spatial coverage is still limited because of the high costs (Wang et al., 2022; Petetin et al., 2018; Tillmann et al., 2022). Satellite retrievals mainly provide the total column of air pollutants, thus providing little information on the vertical distribution of the air pollutant concentrations in the planetary boundary layer (PBL) and at the Earth's surface (Martin, 2008). Consequently, a significant observational gap exists in the PBL, which is the lowest part of the atmosphere characterized by the highest concentrations of air pollutants due to anthropogenic emissions (Scheffe et al., 2009).

Unmanned Aerial Vehicles (UAVs), also known as drones, are comparatively new measurement platforms that have begun to be widely utilized in recent years to obtain in-situ measurements of atmospheric trace gases and aerosols within the lower atmosphere (Schuyler and Guzman, 2017; Yang et al., 2023), bringing many opportunities to improve air pollution monitoring. The increase in drone applications comes mainly from their numerous advantages, such as portability and flexibility while being affordable. In addition, they can provide in-situ observations of various atmospheric constituents with high temporal and vertical resolution (Lawrence and Balsley, 2013). However, drone measurements come along with some limitations as, for instance, flights are complicated during strong wind conditions, require good visibility, and are often restricted to maximum altitudes due to aviation safety reasons. Nevertheless, they can fill the existing observational gap in the PBL and provide valuable information on the distribution of air pollutants.

Several studies present drone campaigns that observed the atmospheric composition and meteorological parameters during the last two decades (Villa et al., 2016; Bretschneider et al., 2022). The measured data, mostly from the PBL region, were used for research on the atmospheric boundary layer (Wang et al., 2021), pollutants variability and distribution (Altstädter et al., 2015; Illingworth et al., 2014), as well as to study the properties of aerosols (Roberts et al., 2008; Corrigan et al., 2008), and to qualify local emissions sources (Nathan et al., 2015). Furthermore, drone campaigns have been conducted in remote areas, such as the Arctic and Antarctic regions (Lampert et al., 2020), as well as during volcano eruptions (Diaz et al., 2012).

To our knowledge, the assimilation of drone observations has only been tested in the context of Numerical Weather Prediction (NWP) models (Flagg et al., 2018; Leuenberger et al., 2020), and no study has yet explored their impact in the case of chemical data assimilation. Meteorological studies have shown that the assimilation of meteorological drone data has a positive impact on improving weather forecasts. This has prompted further ongoing research regarding the possibility of implementing drone observations in support of operational meteorology forecasting and for real-time data assimilation studies (O'Sullivan et al., 2021). Impact studies have revealed a large improvement in the vertical distribution of temperature, relative humidity, and wind as well as a reduction of bias and root-mean-square error (RMSE) when drone observations are assimilated using a variational

data assimilation system within high-resolution NWP models (Jonassen et al., 2012; Flagg et al., 2018; Jensen et al., 2021; Sun
60 et al., 2020; Leuenberger et al., 2020).

Given the positive impact that has been reported in the case of meteorological applications, questions arise about the potential benefits and limitations of drone observations when assimilated within a CTM. In this study, the impact of drone data assimilation on air quality analyses using the regional and high-resolution EURopean Air pollution Dispersion – Inverse Model (EURAD-IM) and the four-dimensional variational (4D-var) data assimilation method is investigated. Vertical profiles of ozone

65 (O_3) and nitrogen oxide (NO) collected during the MesSBAR (Automatisierte luftgestützte **Mes**sung der **S**chadstoff**B**elastung in der erdnahen **A**tmosphäre in urbanen **R**äumen / Automated airborne measurement of air pollution levels in the near earth atmosphere in urban areas) field campaign are assimilated. The potential of drone observations to improve air quality analysis and forecast is explored in a two-day case study by applying the joint optimisation of initial values and emission rates. The aim is to investigate the ability of the 4D-var to adjust local emission rates using vertical profiles that were collected in a region

70 characterised by diverse emission sources. This paper is structured as follows: In Sect. 2, the EURAD-IM and its 4D-var data assimilation system are presented. The MesSBAR field campaign and the experimental design are described in Sect. 3. The results of the 4D-var data assimilation experiments are discussed in Sect. 4. Finally, the summary and conclusions are given in Sect. 5.

2   The modeling system

75   2.1   The EURAD-IM Model

EURAD-IM (**EUR**opean **A**ir pollution **D**ispersion – **I**nverse **M**odel) is a three-dimensional high resolution Eulerian CTM simulating air pollution in the lower troposphere at continental to regional scale. It has been used for several scientific research studies for air quality forecasting, episode scenarios, data assimilation, and inverse modelling (Deroubaix et al., 2024; Gama et al., 2019; Elbern et al., 2007; Duarte et al., 2021; Franke et al., 2022). EURAD-IM is part of the regional Copernicus Atmo-

80 sphere Monitoring Service (CAMS), providing daily air quality forecasts and reanalysis over Europe, which enable continuous quality assurance using observations and inter-model evaluation (Marécal et al., 2015).

Table 1 presents a summary of the specific model settings and modules utilized in the EURAD-IM configuration employed in this study. EURAD-IM describes the transport by diffusion and advection of various trace gas components emitted both by anthropogenic and biogenic sources and considers the gas-phase chemical transformation of about 110 chemical species with

85 265 reactions. The MADE (Modal Aerosol Dynamics model for Europe) module is employed to investigate aerosol dynamics within EURAD-IM, providing information on aerosol size distribution and chemical composition. This module simulates the formation and transformation of both primary and secondary aerosols, considering the interactions between the gas-phase and aerosols. EURAD-IM accounts for the loss of chemical components through wet and dry deposition, as well as aerosol sedimentation. Moreover, EURAD-IM includes a 4D-var assimilation system, as described in the subsequent section, along with

90 the adjoint code derived from the forward code detailed in Elbern et al. (2007). The adjoint model incorporates the transport, diffusion and gas transformation processes of the chemical species as well as secondary inorganic aerosol formation.

Table 1. Summary of EURAD-IM configuration.

	Processes	Modules & References
Transport	Advection	Walcek scheme (Walcek, 2000)
Gas-phase Chemistry	Kinetic Chemistry mechanism	RACM-MIM (Stockwell et al., 1997)
	Dry deposition	Zhang et al. (2003) scheme
	Wet deposition	Roselle and Binkowski (1999)
	Chemistry solver	KPP (Sandu and Sander, 2006)
Aerosols	Aerosol dynamics	MADE (Ackermann et al., 1998)
	Secondary Inorganic Aerosols	HDMR (Rabitz and Aliş (1999))
	Secondary Organic Aerosols	SORGAM (Schell et al., 2001)
Emissions	Biogenic emissions	MEGAN (Guenther et al., 2012)
	Anthropogenic emissions	TNO-UBA emission inventory (Kuenen et al., 2014)
Assimilation	4D-var system	Elbern et al. (2007)
	Minimisation algorithm	L-BFGS algorithm (Liu and Nocedal, 1989)
	Background error covariance modelling	Weaver and Courtier (2001)

The CTM is driven by meteorological fields from the Weather Research and Forecasting model (WRF, version 3.7, Skamarock et al. (2008)) as thermo-dynamical forcing. The ECMWF (European Centre for Medium-Range Weather Forecasts) IFS (Integrated Forecasting System) global analysis (ERA5) is used for initialization and boundary conditions for the WRF simulations.

95 Chemical boundary conditions are generated by the CAMS global reanalysis data set (EAC4) that is produced by the ECMWF Composition Integrated Forecasting System (C-IFS). Anthropogenic emissions used for this study are provided by the German Environment Agency (Umweltbundesamt, UBA) for Germany and by the TNO-MACC-II inventory (Kuenen et al., 2014) for the rest of Europe. The emissions data set is subject to processing in the EURAD Emission Module (EEM) (Memmesheimer et al., 1995) for seasonal and diurnal redistribution, as well as attributions to working days and weekends. The emission data is

100 divided into point and area sources. The data contains emissions of gaseous air pollutants, i.e., carbon monoxide (CO), nitrogen oxides (NOx), sulfur dioxide (SO_2), total non-methane volatile organic compounds(NMVOC), and ammonia (NH_3), and for aerosols PM_{10} (particulate matter with a diameter < 10 μm) and $PM_{2.5}$ (particulate matter with a diameter < 2.5 μm) emissions. Biogenic emissions are calculated online using the Model of Emissions of Gases and Aerosols from Nature (MEGAN), while wild fire emissions are not considered here and did not play a role in the investigated case.

105 ## 2.2 4D-Var data assimilation

The EURAD-IM data assimilation system is based on the 4D-Var method as described in Elbern and Schmidt (2001) and Elbern et al. (2007). The 4D-var approach aims to determine the optimal model state by combining the prior information (e.g., provided by a forecast) with observational data over an assimilation window through the minimization of the following cost

function $\mathbf{J}$

$$110 \quad \mathbf{J}(\mathbf{x_0}, \mathbf{e}) = \frac{1}{2}(\mathbf{x_0} - \mathbf{x}^b)^T \mathbf{B}^{-1}(\mathbf{x_0} - \mathbf{x}^b) + \frac{1}{2}\sum_{i=0}^{n}((\mathbf{y}_i - \mathbf{H}_i\mathbf{M}_i\mathbf{x_0})^T \mathbf{R_i^{-1}}(\mathbf{y}_i - \mathbf{H}_i\mathbf{M}_i\mathbf{x_0})) + \frac{1}{2}(\mathbf{e} - \mathbf{e}^b)^T\mathbf{K^{-1}}(\mathbf{e} - \mathbf{e}^b). \quad (1)$$

Here, the optimisation is subject to the initial conditions $\mathbf{x}_0$ and the emission correction factor $\mathbf{e}$. As a result, the cost function formulation includes an additional element (in contrast to the usual 4D-var used for NWP) that accounts for emissions. The model state is mapped from the model space to the observation space by the observation operator $\mathbf{H}_i$ and the model operator $\mathbf{M}_i$, producing the model equivalents of each observation y_i. The matrices $\mathbf{B}$, $\mathbf{R}$, and $\mathbf{K}$ represent the error covariance

115 matrices associated with the a-priori state vector x^b, the observations y_i, and a-priori emissions e^b, respectively. The matrix $\mathbf{R}$ considers only diagonal elements (i.e., it ignores any error correlation between different observations) while accounting for the uncertainties in the measurements and model representation error. The matrix $\mathbf{B}$ is estimated using error variances and the diffusion operator proposed by Weaver and Courtier (2001). Thus, $\mathbf{B}$ can be factorized as $\mathbf{B} = \mathbf{B}^{1/2}\mathbf{B}^{T/2}$ for use in the preconditioning of the highly underdetermined data assimilation system. The matrix $\mathbf{K}$ is specified as a block diagonal, as

120 presented in Paschalidi (2015). The minimization of the cost function $\mathbf{J}$ is performed through an iterative process using the Quasi-Newton limited memory L-BFGS algorithm (Liu and Nocedal, 1989), which includes the iterative integration of the forward and adjoint EURAD-IM.

3 The MesSBAR campaign analysis

3.1 Air quality measurements

125 The MesSBAR field campaign took place near Wesseling, Germany, on 22-23 September 2021. During these two days, a multicopter system composed of a drone and a set of low-cost air quality monitoring instruments was used to carry out vertical profile measurements of air pollutants during the early morning hours.Among the instruments loaded in the multicopter, electrochemical sensors were used to monitor nitrogen oxide (NO), and a Personal Ozone Monitor (POM) was employed for assessing ozone (O3). The feasibility of using these sensors for measurements in the planetary boundary layer was discussed

130 in (Schuldt et al., 2023; Tillmann et al., 2022). A detailed description of the development, technical characteristics, and calibration of the multicopter system can be found in Bretschneider et al. (2022). The campaign's basis was located within the proximity of the A555 highway, which is a much-frequented connection between the German cities of Cologne and Bonn. The measurements were conducted above agricultural land located about 1 km south of the town of Wesseling. The city centres of Cologne and Bonn are about 15 km north and 10 km south of the measurement location, respectively (Fig.1). The Wesseling

135 region is located within the Rhineland chemical region and is widely recognized as a leading chemical hub in Europe. Wesseling, in particular, hosts a remarkable level of industrial activity attributed to the presence of major companies operating in the chemical and petroleum sectors (source: https://www.chemcologne.de/en/investments/the-rhineland-chemical-region, access date: February 21,2024).

The objective of this campaign was to capture the early morning evolution of air pollutant concentrations with the development
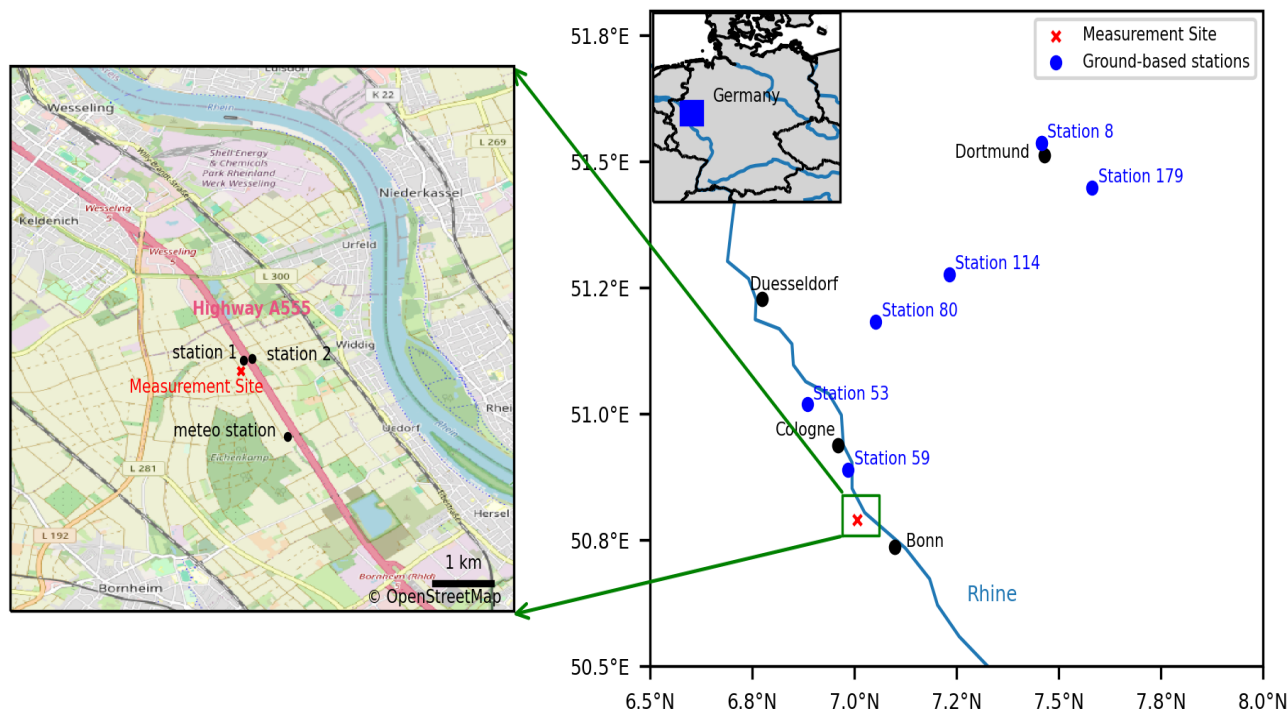
Figure 1. Geographic map displaying the MesSBAR measurement location, air quality ground stations, and meteorological station situated near the A555 highway. Source: OpenStreetMap

of the PBL. Furthermore, the proximity to the highway allows for measurements of pollutants specifically originating from traffic sources.

The flights were performed with a continuous ascending speed of approximately 1 ms^{-1}, reaching a maximum altitude of 350 m. This altitude limitation was imposed by air traffic restrictions in the area due to its proximity to the Cologne/Bonn airport. During each drone flight, two profiles were acquired: the ascent and the descent. For assimilation experiments within EURAD-IM, only the ascent profiles were utilized due to their higher accuracy. In this study, the vertical profiles of ozone (O$_3$) and nitrogen monoxide (NO) obtained from the multicopter are utilized and assimilated within EURAD-IM. Additionally, observations from two ground-based stations situated on both sides of highway A555 are used to validate the simulation results. Furthermore, meteorological observations from an automatic weather station, located approximately 1 km south-east from the measurement site, are employed for comparing meteorological data, especially the wind field.

3.2 Simulations setup

The objective of this study is to investigate the impact of O$_3$ and NO drone profile assimilation on the air quality analysis using high-resolution EURAD-IM simulations. The model grid has a horizontal resolution of 5 km × 5 km and is vertically

divided into 30 layers defined by terrain following sigma coordinates between the surface and 100 hPa, with about 19 layers covering the lowest 1 km of the atmosphere. The EURAD-IM domain covers central Europe, including Germany with 271 x 298 grid points. The model output is adjusted to provide forecasts with a temporal resolution of 60 s, allowing for more precise comparison with the high-resolution drone observations. To assess the impact of drone data assimilation on air quality forecast, simulations are conducted both with and without data assimilation (Table 2). The joint initial value/emission rate optimisation mode of EURAD-IM is activated for this purpose. Two 24-hour experiments are performed without assimilation: one on 22 September 2021, and the other on 23 September 2021. In these experiments, the model is initialized with a climatology state with a spin-up time of 6 days (16-21 September 2021) prior to the campaign dates in order to establish a chemically balanced initial state. Moreover, two additional simulations focusing on O_3 and NO data assimilation are performed for 24 hours, covering the same period as reference simulations without data assimilation. The assimilation window is deliberately selected to coincide with the availability of observations, aiming to minimize computational time in the simulations while also ensuring a meaningful lead time for emission optimisation.

Table 2. Model simulations presented in this paper.

Experiment name	Assimilation	Period	Assimilation Window	Assimilated Observations
REF_22SEP	no	24-hour period on 22 September 2021	-	-
REF_23SEP	no	24-hour period on 23 September 2021	-	-
DA_22SEP	yes	24-hour period on 22 September 2021	00-11 UTC	6 drone profiles of O_3 and NO
DA_23SEP	yes	24-hour period on 23 September 2021	00-09 UTC	5 drone profiles of O_3 and NO

165 ## 3.3 Evaluation of the wind situation
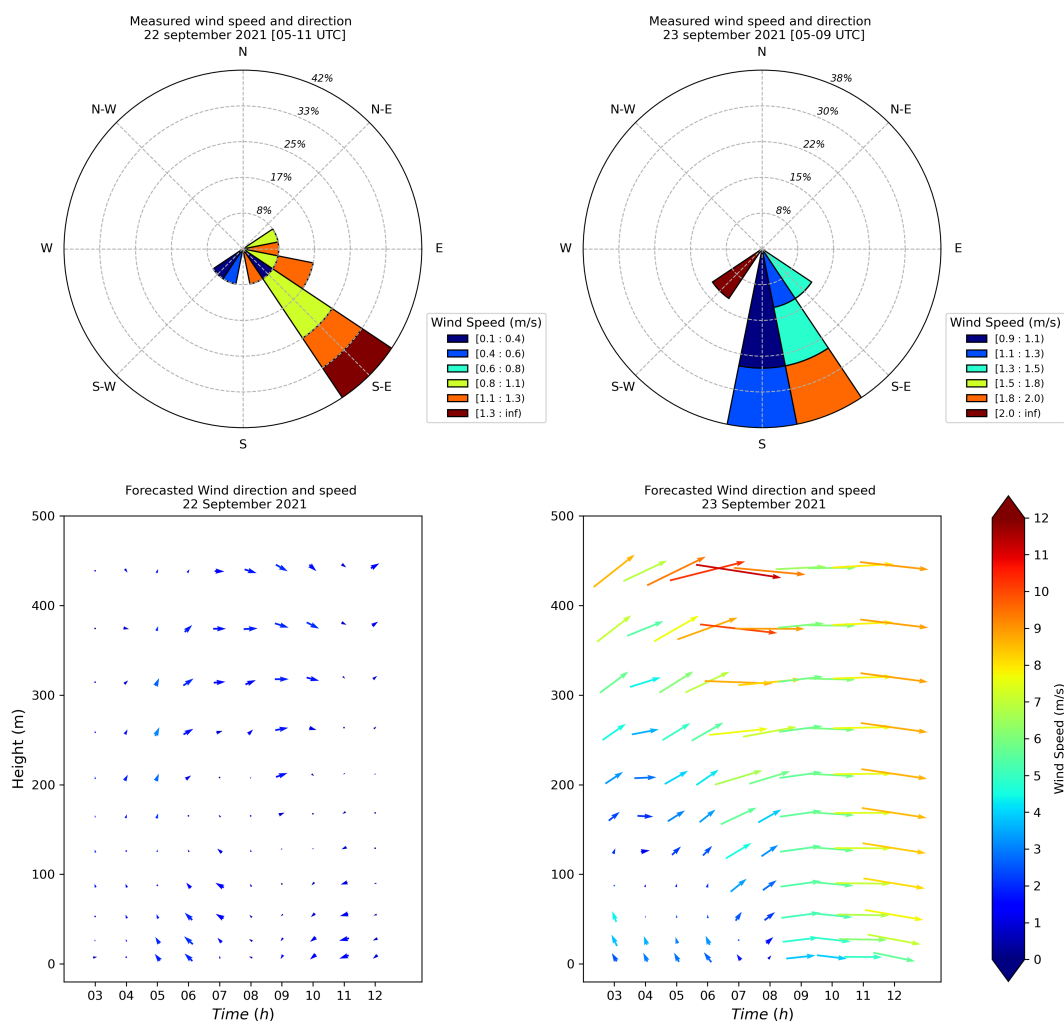
Figure 2. Observed surface wind speed and direction during the measurement period on 22 September 2021 (upper left) and 23 September 2021 (upper right).Forecast of horizontal wind profiles for different hours for the lowest 500m on 22 September 2021 (bottom left) and 23 September 2021 (bottom right).

The wind patterns are critical parameters that govern the dispersion of air pollutants and their transport, with a direct influence on emissions optimisation within the framework of inverse CTMs. The wind conditions at the observation site are evaluated for two purposes: firstly, to validate the suitability of the measurement site location for measuring local traffic emissions, and secondly, to assess the horizontal wind for applications to emission optimisation.

170 Figure 2 shows the surface wind speed and direction observed by the weather station during the flights' operation hours. The dominant wind direction is primarily from the south-east during the first day, with a maximum speed of 1.3 ms^{-1}, while it

comes from the south to south-east on the following day, with a maximum recorded speed of 2.0 ms^{-1}. This indicates that the observation point is strategically located downwind of the nearest traffic emission source, which enabled the multicopter to successfully capture the emissions from the highway.

175 Apart from the surface conditions during the measuring period, the two days are characterized by a distinct wind situation, as shown in the horizontal wind profiles extracted from the WRF simulations in Fig. 2. On the first day, the wind patterns exhibit vertical wind shear throughout the day and across all levels, changing direction from the southeast/east at lower altitudes to the west/northwest at higher altitudes. However, the wind intensity remains relatively low, measuring less than 3.0 ms^{-1}. On the following day, the surface wind direction aligns with the observations during the campaign period. Nevertheless, at higher

180 levels and beyond the campaign period, westerly and south-westerly winds dominate, and their speed increases with height. The maximum speed is reached at 450m with 12.0 ms^{-1}. These different horizontal wind profiles between the two days may result in variations in terms of assimilation outcomes, particularly with respect to emission optimisation. Therefore, the results of the assimilation experiments are discussed, considering the specific characteristics of each of the two days.

4 Results

185 ### 4.1 Impact on vertical profiles

In order to evaluate the impact of drone data assimilation on the air pollutant's vertical distribution and given the lack of independent vertical profiles, the simulation results are first compared to the drone observations that are assimilated. Figure 3 presents the observed O_3 and NO drone profiles as well as vertical profiles resulting from the 4D-var assimilation analysis and the reference simulations for all assimilated profiles. For both days, the 4D-var analyses agree better with the drone observations

190 in comparison to the reference forecast for both species, which indicates the successful assimilation of the drone observations. On 22 September 2021, an underestimation by the reference simulation is observed for the O_3 levels at altitudes above 200 m, with discrepancies reaching up to 15 ppb, especially for the first three flights (F1, F2, and F3). The assimilation of drone vertical profiles significantly reduces this underestimation by 45% on average. On 23 September 2021, the reference model run overestimates the O_3 concentration at the ground and near-surface levels. The largest overestimation is visible for the first

195 three flights of the day (F7, F8, and F9) by about 20 ppb. Due to the 4D-Var assimilation, the O_3 ground bias is reduced by more than 85%. Consequently, biases in O_3 concentration are reduced by nearly 30% on the first day and 55% on the second day (Table 3).

For the NO forecast on both days, the reference simulations underestimate the NO vertical distribution at all heights, with the strongest discrepancies at ground level. Improvement due to the assimilation is accomplished mostly at surface and near-surface

200 levels for the initial three flights of each day (F1, F2, F3, F7, F8, and F9), with more pronounced adjustments on the second day, resulting in a bias decrease of up to 84% at ground level. For higher levels, the impact of the assimilation is minimal to non-existent, for instance, for the flights F7 and F8 above 150 m. Contrarily, because the pollutant concentrations are well mixed in the PBL, a uniformly positive impact throughout the vertical can be seen in the NO analyses of the latest flights of the day (F4, F5, F6, F10, and F11). Overall, the 4D-var assimilation of drone observations leads to a substantial reduction of

205 more than 35% in NO biases between the reference model forecast and observations on both days (Table 3).

These results highlight the successful assimilation of drone observations by the EURAD-IM 4D-var system. The accuracy of these findings is further examined and discussed in Sect. 4.3 through a validation process using independent observations.

Table 3. O_3 and NO biases (model value minus observation) in ppb for each flight.

Model runs	O_3 Vertical Profiles							NO Vertical Profiles						
	F 1	F 2	F 3	F 4	F 5	F 6	Daily bias	F 1	F 2	F 3	F 4	F 5	F 6	Daily bias
REF_22SEP	-4.65	-2.06	-3.53	-1.23	-0.91	-2.49	2.48	-27.96	-35.39	-39.34	-28.21	-28.11	-30.09	31.52
DA_22SEP	0.07	-1.32	-2.09	-0.38	-2.42	-4.20	1.75	-21.18	-23.78	-30.43	-17.40	-12.85	-15.43	20.18
	F 7	F 8	F 9	F 10	F 11		Daily bias	F 7	F 8	F 9	F 10	F 11		Daily bias
REF_23SEP	15.20	5.12	3.81	3.64	3.86		6.33	-13.95	-20.75	-26.65	-28.03	-30.88		24.05
DA_23SEP	2.71	-2.26	-2.85	-3.92	-2.63		2.87	-9.78	-10.65	-11.37	-20.55	-25.30		15.53
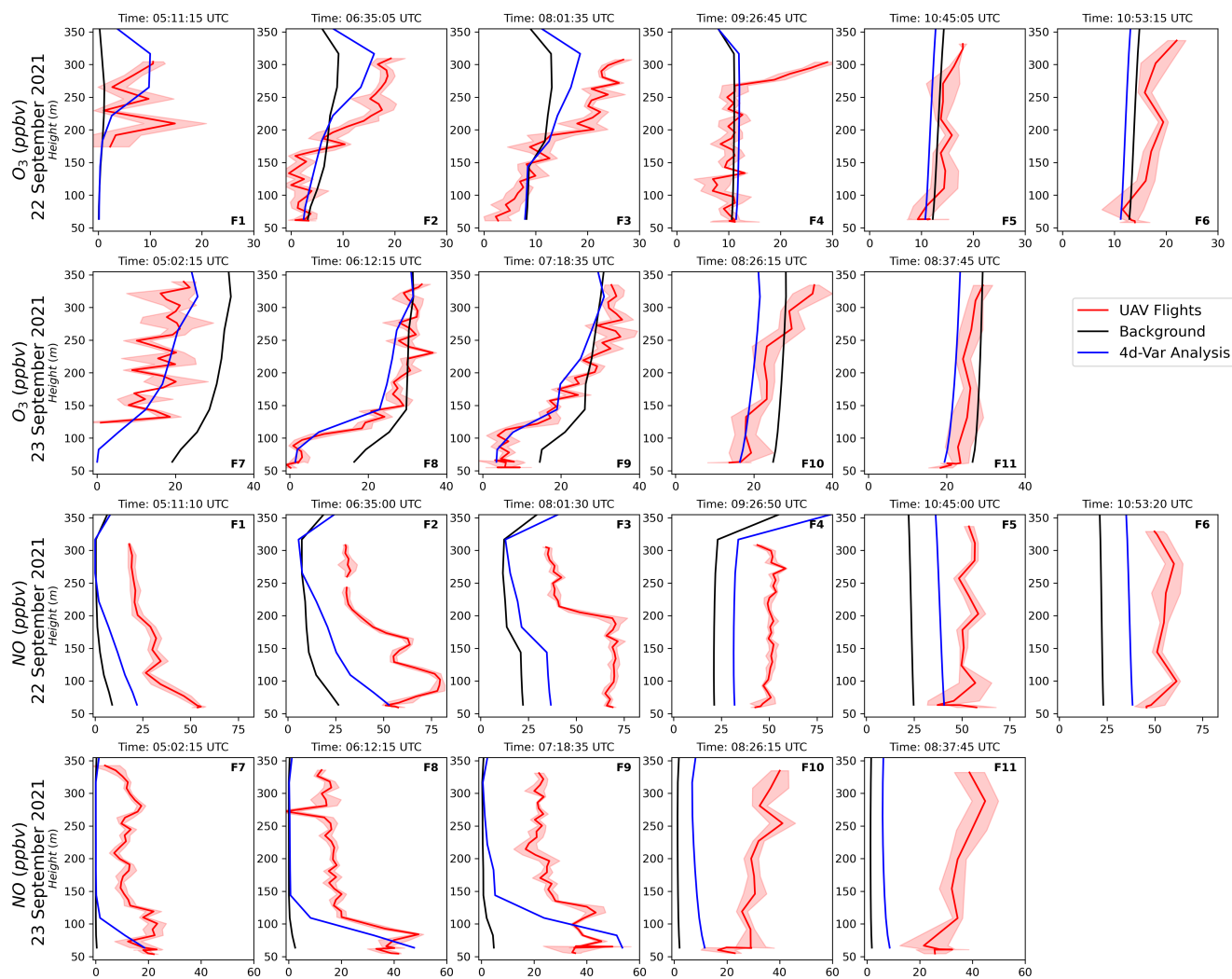
Figure 3. The vertical profiles of O$_3$ and NO measured by the drone system (red line), compared to the 4D-var analysis (blue line) and the reference run (black line) for all flights on 22-23 September 2021. The red shading highlights the standard deviation of the drone observations.

4.2 Emission optimisation

In the present study, the drone observations are assimilated using the joint optimisation of initial value and emission rates, which
210 results in the optimised atmospheric state and the optimisation of correction factors for 25 anthropogenic emitted species. The inversion outcomes are expressed as emission correction factors, which represent the ratio between the optimised emission rates and the input emission rates for each species. Emission factors with a value of 1 indicate that the optimised emissions are equal to those of the input, while a factor higher (or smaller) than 1 signifies an increase (or decrease) in emissions.

Figure 4 shows the emission correction factors of NO and NO_2 for both days of the study. Particularly, these two species exhibit
215 the highest emission correction factors. Given their correlation with NOx emissions, carbon monoxide CO, sulfur dioxide SO_2, and sulfate SO_4 have also been optimised and reveal emission correction factors ranging between 1 and 2 for DA_22SEP and between 1 and 3 for DA_23SEP. No significant emission corrections are noticed for the remaining species (not shown). There are two main differences noted between the two days' results. Firstly, the NO and NO_2 emission correction factors resulting from DA_23SEP are 4 to 5 times higher than those of DA_22SEP. Secondly, a subtle discrepancy is evident in the spatial
220 distribution of the emission correction factors. Figure 5 presents the original and optimised total NOx emissions across the region as well as the difference between them. For DA_22SEP, an increase of NOx emissions (up to 16 Mg per day) is noted in the grid cells surrounding the observation point, with a maximum increase located north of the measurement point. This can be attributed to the wind characteristics and local emission sources. On that day, the surface winds are weak and exhibited high variability, with speeds remaining below 1.5 ms^{-1}, which constrained the air pollution transport. Conversely, at higher
225 altitudes, the strongest wind speeds are observed predominantly from the west and north-west. Furthermore, precisely to the north and north-west of the measurement site, there are emission point sources associated with industrial activities and energy production (Fig. A1, Fig. A2). Therefore, the rise in NOx emissions on the first day is primarily associated with the industry and energy sectors, while the transport sector is less affected.

In the case of DA_23SEP, the results vary from those of the previous day, with a larger increase in emissions occurring in
230 an area characterized by initially low emission levels (up to 40 Mg per day). Unlike in DA_22SEP, the highest increase in emissions is located south and south-west of the campaign location as a consequence of the strong winds blowing from south-east and south-west on that day. Therefore, an increase in emissions from the road transport sector and, to a lower degree, the industrial and energy sectors are noted in DA_23SEP.

From these results, it can be seen that the emission optimisation is strongly linked to the wind characteristic during the as-
235 similation window. This aligns with the findings of Wu et al. (2022), demonstrating that under optimal wind direction or diffusion conditions, efficient optimisation in emissions can be achieved when the observation configuration is above ground level. Therefore, two main conclusions can be drawn from the evaluation. Firstly, NOx emissions need to be elevated in the examined area. Secondly, the 4D-var assimilation system successfully used the information contained in the drone observations for emissions optimisation. This suggests that the drone observations can be valuable in the process of optimising local
240 emissions.
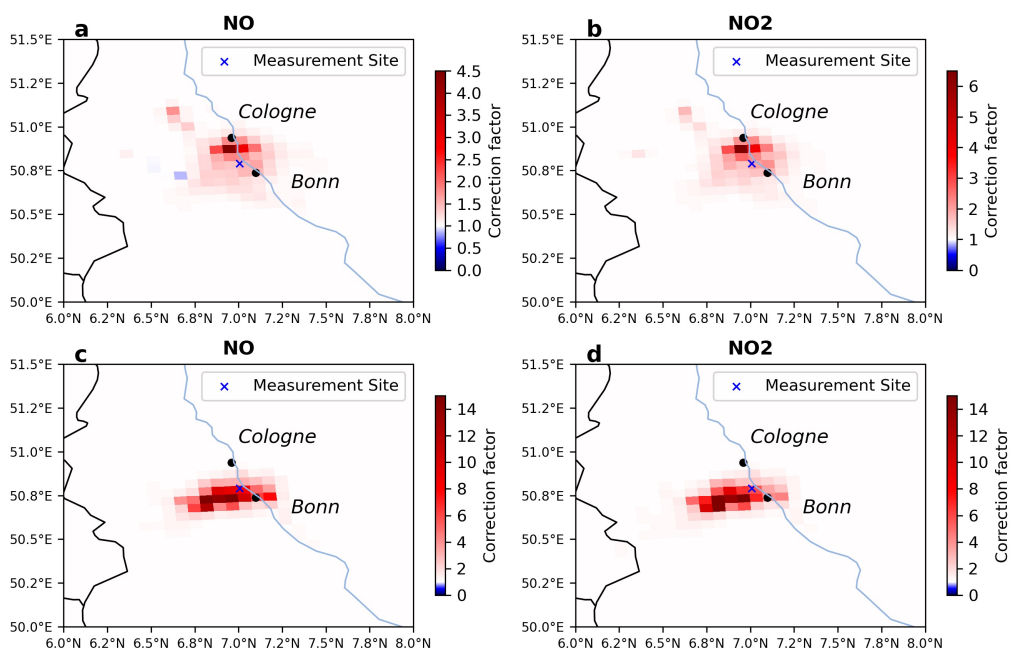
Figure 4. Emission correction factors of NO and NO$_2$ resulting from the conducted assimilation experiments on 22 September 2021 (a and b) and 23 September 2021 (c and d).
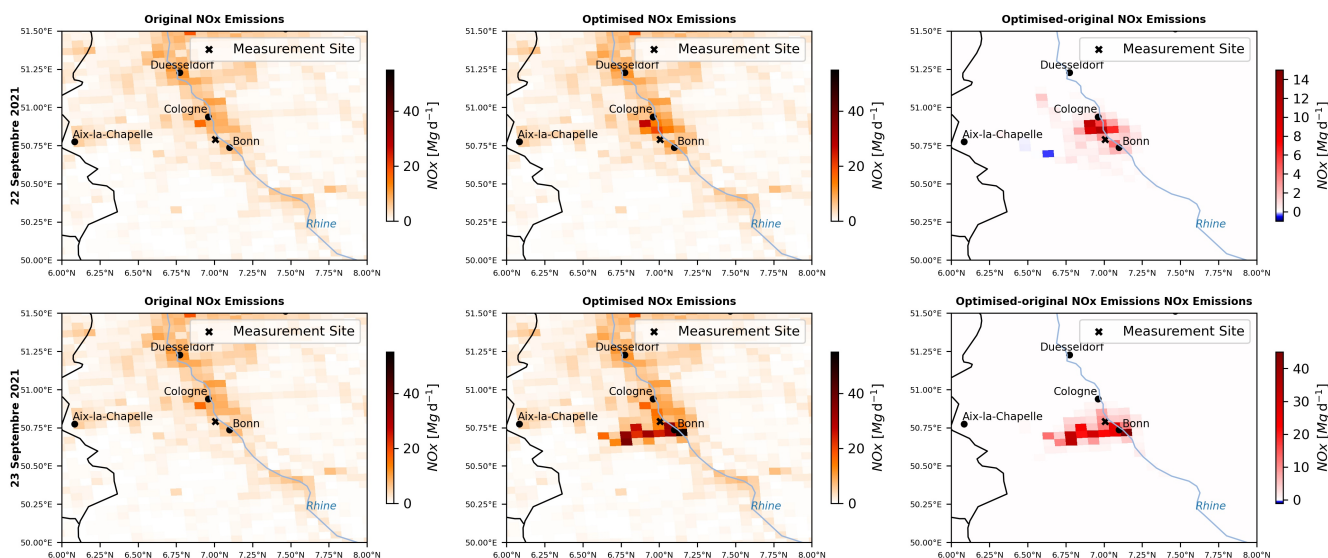
Figure 5. NOx emissions from the original emissions inventory (left), the optimised emissions resulting from the data assimilation simulations (middle), and the difference between the original and optimised emissions (right).

4.3 Validation against independent observations

4.3.1 Local impact

To validate the impact of the drone data assimilation, we compare the experiment results with independent ground-based observations. These observation sites are located in the same grid cell as the assimilated data and were obtained from two

245 monitoring stations located one on each side of the A555 highway (Fig. 1). Figure 6 shows the daily time series of observed O_3, NO, and NO_2 concentrations along with the modelled concentrations from both the reference and assimilation experiments. To evaluate the benefits of the data assimilation, the bias, RMSE (Root Mean Square Error), and Pearson correlation (R) is examined for all experiments averaged over the assimilation window and over a 24-hour period (Table 4), using the means of the observations of the two stations as reference.

250 The DA_22SEP experiment performance for the O_3 concentrations is almost similar to the reference experiment. Following the analysis of Sect. 4.1, this is expected because of the initial good agreement between the a priori forecast and the drone observation for near-ground O_3 concentration during this day. The main improvement during the first day is seen for the NO concentrations within the assimilation window as well as during the subsequent free forecast. The assimilation of drone observations results in a strong reduction of the bias by 87% and the RMSE by 20%, with an amelioration in the Pearson

255 correlation by 0.15 over a 24-hour period. The daily NO_2 cycle is impacted by the assimilation due to its chemical coupling with O_3 and NO. The assimilation experiment exhibits a better performance during the daytime relative to the reference experiment. However, during the late afternoon and nighttime, the reference experiment performs better than DA_22SEP, as NO_2 is slightly overestimated. The best performance of the drone data assimilation results is obtained on the following day. A remarkable improvement in the O_3 concentration is noticed within the initial seven hours of the day. The bias is reduced by

260 60% and the RMSE by 45%, which also results in an improvement of the correlation by 0.22 over the assimilation period. A better improvement in the assimilation results is achieved for NO concentrations. The assimilation experiments reduce the bias by 50% and RMSE by more than 27%, with an amelioration in the correlation by 0.5 over the 24-hour evaluation period. For NO_2, a notable improvement can be seen in the forecast from DA_23SEP compared to the REF_23SEP. Within the assimilation window, the bias was reduced by 43%, the RMSE by 29%, and the correlation improved by 0.19.

265 These results indicate that the 4D-var assimilation of the drone observations has the potential to improve concentration of O_3, NO, and NO_2 during the daytime when optimising both the initial values and emissions rates simultaneously. Moreover, the reduced bias for both NO and NO_2 confirms that the increase in NOx emissions seen in the nearby grid cell (Fig. 5) is a good result, especially in the case of 23 September 2021.

The observed decline in daytime surface O3 concentration in both assimilation runs is relarted to the NOx titration process.

270 The optimisation of emission correction factors has led to an increase in NOx emissions within the analysed grid cell, which enhanced the rapid reaction between O_3 and NO, resulting in the formation of NO_2. As a consequence, there is a reduction in the simulated surface ozone. According to Sillman (1999), this daytime ozone removal is typically prominent in areas characterised by significant NO emission sources, especially large point sources. In our specific case, the analysed grid cell demonstrates elevated levels of NOx emissions, primarily originating from both traffic and industrial sources. In the DA_23SEP
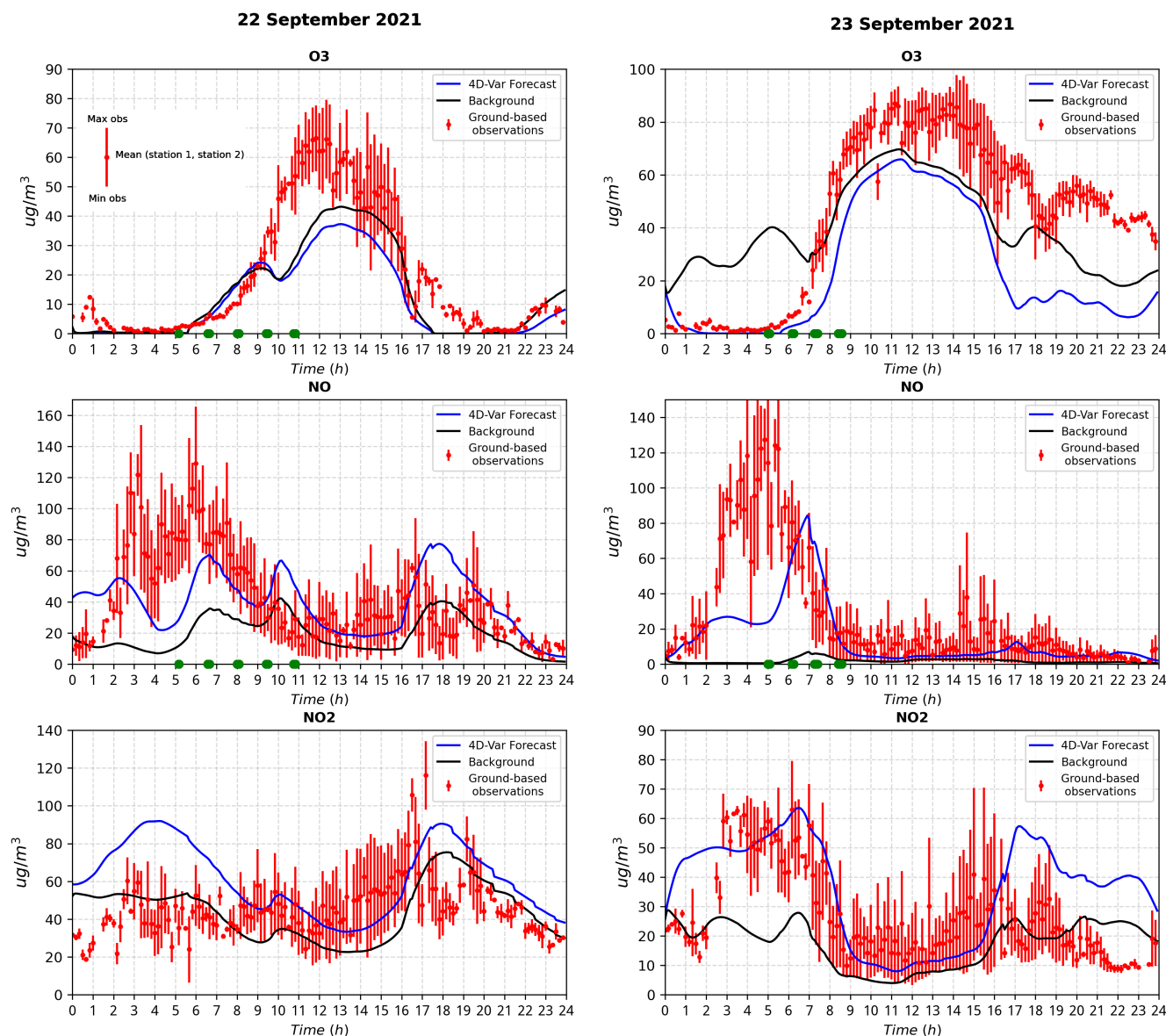
Figure 6. Temporal evolution of the O$_3$, NO, and NO$_2$ concentrations as observed by the ground-stations (red line) and given by the model in the corresponding grid cell: the background (black line) and the analysis (blue line) over the 24-hour forecast period on the two days of the campaign. Green dots highlight the time of the assimilated drone profiles.

experiment, the model's suboptimal performance in the free run is likely attributed to an overestimation of NOx titration, given the absence of ozone formation and the predominance of NOx titration as the primary process during the nighttime. This leads to a noticeable decrease in O$_3$ concentration and a simultaneous increase in NO$_2$ concentrations during nighttime periods.

Table 4. Statistical comparison of ground observations and model outputs (Bg: reference run, Ana: assimilation run) for O_3, NO, and NO_2 within the assimilation window (and for 24h-forecast) during the two studied days. The Bias and RMSE are in μgm^{-3}.

	Statistics	O_3		NO		NO_2	
		Bg	Ana	Bg	Ana	Bg	Ana
22 Sep 2021	Bias	-3.91 (-6.02)	-4.37 (-8.50)	-39.93 (-23.45)	-14.52 (-2.97)	2.97 (-1.40)	27.17 (15.73)
	RMSE	10.52 (11.42)	10.93 (13.73)	53.17 (37.84)	38.44 (30.14)	13.90 (17.66)	32.08 (26.10)
	Corr	0.83 (0.92)	0.81 (0.92)	-0.14 (0.13)	-0.10 (0.28)	-0.13 (0.20)	0.16 (0.18)
23 Sep 2021	Bias	18.53 (-5.37)	-7.35 (-21.60)	-52.62 (-24.82)	-23.61 (-11.75)	-17.83 (-9.45)	10.06 (8.99)
	RMSE	24.10 (21.91)	13.04 (26.32)	66.16 (41.77)	46.93 (30.18)	22.84 (17.40)	16.16 (18.70)
	Corr	0.70 (0.71)	0.92 (0.86)	-0.28 (-0.07)	0.22 (0.56)	0.40 (0.28)	0.59 (0.49)

4.3.2 Regional impact

In the previous validation, the impact of the data assimilation on the same model grid cell as the data being assimilated is
280 evaluated. To further investigate the effect on a larger spatial scale, an additional validation is performed using independent ground-based observations from six different ground-based air quality monitoring stations situated in the vicinity of the observation site (Fig. 1, Table A1). For this validation, stations that are impacted by the assimilation are selected. They are located at distances ranging from 12 km to 85 km away from the campaign location. Given the unavailability of NO observations, this validation considers only O_3 and NO_2. Although NO_2 is not assimilated in this study, it is indirectly influenced due to chemical
285 coupling with the observed species and via the emission optimisation. Figure 7 presents the hourly RMSE time series of the O_3 forecast for the assimilation and reference experiments, averaged over the selected stations. The RMSE of O_3 and NO_2 within the assimilation window, for all simulations per station, are presented in Table 5.

Figure 7 shows that the O_3 RMSE for DA_22SEP and DA_23SEP is notably lower than that of the reference simulations within the data assimilation window. Outside the assimilation window, only a small added error is noted between 11 and 17 UTC for
290 DA_22SEP, which appears similar to the results of the local validation, while no impact is observed during the subsequent free forecast period for DA_23SEP. The largest RMSE reduction takes place at Station 59 (30% in 22 September and 40% in 23 September) and Station 80 (35% in 22 September and 34% in 23 September), situated 12 km and 43 km north of the observation site, respectively. The smallest reduction occurs at the stations of furthest distance, namely at Station 8 (5.21% in 22 September and 3.78% in 23 September) and Station 179 (2.61% in 22 September and 6.95% in 23 September), which are
295 approximately located 85 km north-east of the campaign site. These results suggest that the positive impact of the drone data assimilation is transported to a broader area surrounding the campaign location, resulting in an improvement of O_3 concentrations across a larger area.

For NO_2, a significant RMSE reduction is found at Station 80 (72.44%) located 43 km north of the campaign site for DA_22SEP. However, the RMSE for Station 59 and Station 53 show an increase within the assimilation window. For DA_23SEP,
300 better results can be seen for all stations except for the rural Station 59. The best reduction is at the Stations 80 (21.24%) and 114 (21.86%).

Despite the simplicity of the current assimilation approach, which only incorporates data from a single grid box, a positive effect of assimilation is apparent even for stations situated at larger distances from the campaign's location. This is attributed to the transport of the increment throughout large areas of the studied region.
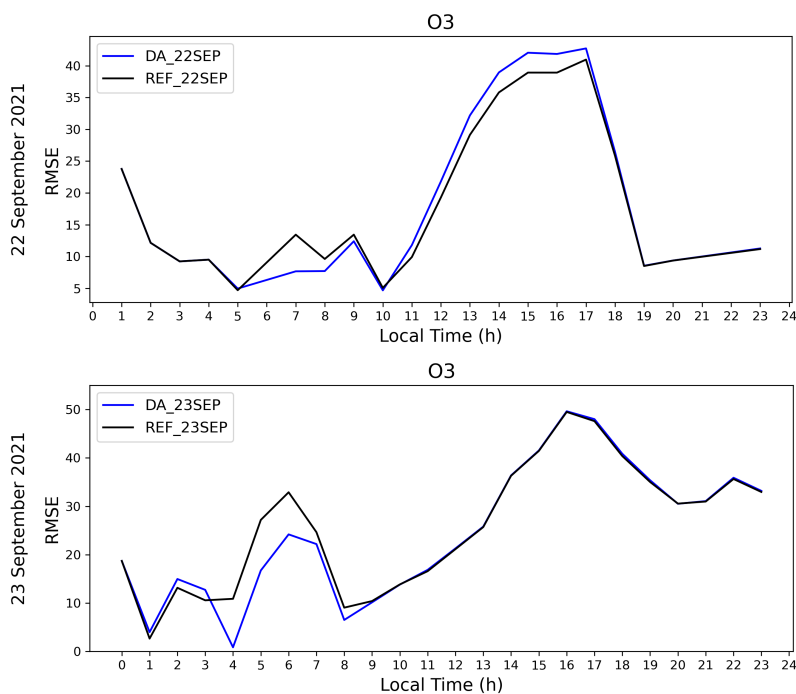
Figure 7. Temporal evolution of the RMSE (model-observations) in ppbv for O_3 calculated for the background (black) and the analysis (blue) over the 24-hour forecast period across all ground stations on 22 September 2021 (top) and 23 September 2021 (bottom).

Table 5. The O_3 and NO_2 RMSE between observations data and model results obtained with assimilating drone data and without assimilation. The results are shown for every ground-based station for the assimilation window. The RMSE is in *ppbv*.

RMSE		DA Window		DA Window	
		REF_22SEP	DA_22SEP	REF_23SEP	DA_23SEP
	Station 8	11.33	10.74	12.17	11.71
	Station 53	10.29	9.66	8.19	7.29
O_3	Station 59	7.75	5.49	16.71	10.1
	Station 80	6.35	4.13	14.58	9.6
	Station 114	25.86	24.39	22.69	19.87
	Station 179	27.96	27.23	17.55	16.33
	Station 8	18.11	17.49	24.05	22.92
	Station 53	12.85	23.81	10.26	10.77
NO_2	Station 59	24.25	44.34	16.88	24.45
	Station 80	10.63	2.93	19.59	15.43
	Station 114	24.14	25.82	12.81	10.01
	Station 179	17.78	18.04	19.85	18.08

305 ## 4.4 Analysis of differences in the assimilation results

Table 6. The percentage of cost reduction achieved for O_3 and NO, as well as the percentage of the partial costs attributed to initial value correction (IV) and emissions correction (EF).

	Cost reduction		Partial costs	
	O_3	NO	EF	IV
DA_22SEP	34%	41%	9%	25%
DA_23SEP	80%	36%	10%	4%

The analysis of the DA_22SEP and DA_23SEP experiments shows that the assimilation of drone observations has a positive impact on the vertical distribution of O_3 and NO, and on the daily cycle of O_3 and NOx at ground level. The results reveal differences in the performance of the analysis between the two experiments. This discrepancy is particularly noticeable for the emission correction factors, which are much stronger during the second day. In order to elucidate the underlying cause of this 310 disparity, it is necessary to further analyse the assimilation process in the context of joint initial values/emissions rate optimisation. Table 6 lists the cost reduction in percentage for O_3 and NO, as well as the percentage of the partial cost attributed to the optimisation of the initial values (IV) and the optimisation of the emissions correction factors (EF). For both assimilation experiments, the costs are reduced by more than 30 %, which confirms the successful assimilation of the drone profiles. In particular, the O_3 costs of DA_23SEP are highly reduced by 80 %, resulting in a precise alignment between the 4D-var analysis 315 and the O_3 observations.

The partial costs vary between the two days. For DA_22SEP, the costs associated with IV are more than twice that of EF (25% for IV against 9 % for EF), which indicates important initial value adjustments. In contrast, the opposite is true for DA_23SEP where the effect of optimising the emissions is much higher (4% for IV against 10 % for EF). Figure 8 illustrates the NO analysis increment (4D-var analysis - reference run) at ground level for different time steps for the two assimilation

320 experiments. The increment at the initial time step (00 UTC) provides major insights into the optimisation of initial values. For the DA_22SEP, a strong increase in the NO initial values is noticed in the southeast of the campaign site. This is induced by the winds coming from this direction on this day. It gradually diminished over time, giving precedence to the effect of the emission optimisation. For DA_23SEP, only a minor adjustment is applied to the initial values at ground level, which quickly dissipated. Therefore, the successful optimisation of emissions rates is the principal cause of the analysis improvements for the

325 experiment DA_23SEP.

Another finding that stands out from the results reported in Sect. 4.1 is the limited impact on the NO vertical profiles, particularly evident on the second day. Although effective correction was achieved for ground and near-ground NO levels, limited improvements were observed in the NO concentration at higher altitudes (above 150m) for the first 3 profiles of the day. In Figure 9, the vertically resolved analysis increment for O_3, NO, and NO2 on September 23, 2021, is illustrated. We note a

330 negative ozone increment alongside a positive NO2 increment, both exhibiting a well-developed vertical spread. In the case of NO, its increment is constrained near ground level during the early hours of the day. The reason behind this is the NOx titration process, where freshly emitted NO, including additional NO emissions resulting from emission optimisation, reacts with O_3 to produce NO_2. During the night, as there is neither ozone formation nor photolysis of NO_2, NOx titration becomes the dominant process and leads to the removal of the ozone. Consequently, large improvements are achieved for the O_3 vertical distribution

335 as presented for Flights F7, F8, and F9 (Fig. 3) as well as for the O_3 ground concentrations during the nighttime (Fig. 6). This improvement is primarily attributed to emissions optimisation, as previously explained. However, due to the large initial bias between the background and the assimilated drone observations, an adjustment of the initial values is necessary in order to correct the NO concentration at high altitudes. Unfortunately, for this study case, the assimilation of drone data from a single grid cell proved insufficient to achieve a strong initial values correction.
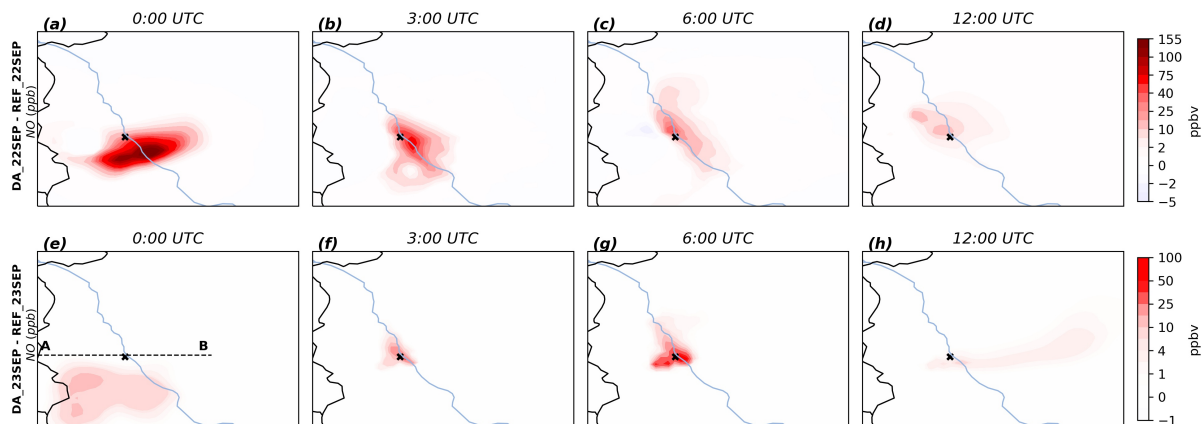
Figure 8. Analysis increment of NO at ground level on 22-23 September 2021 at selected time steps. In panel (e), the dashed line between **A** and **B** indicates the cross-section being presented in Fig. 9.
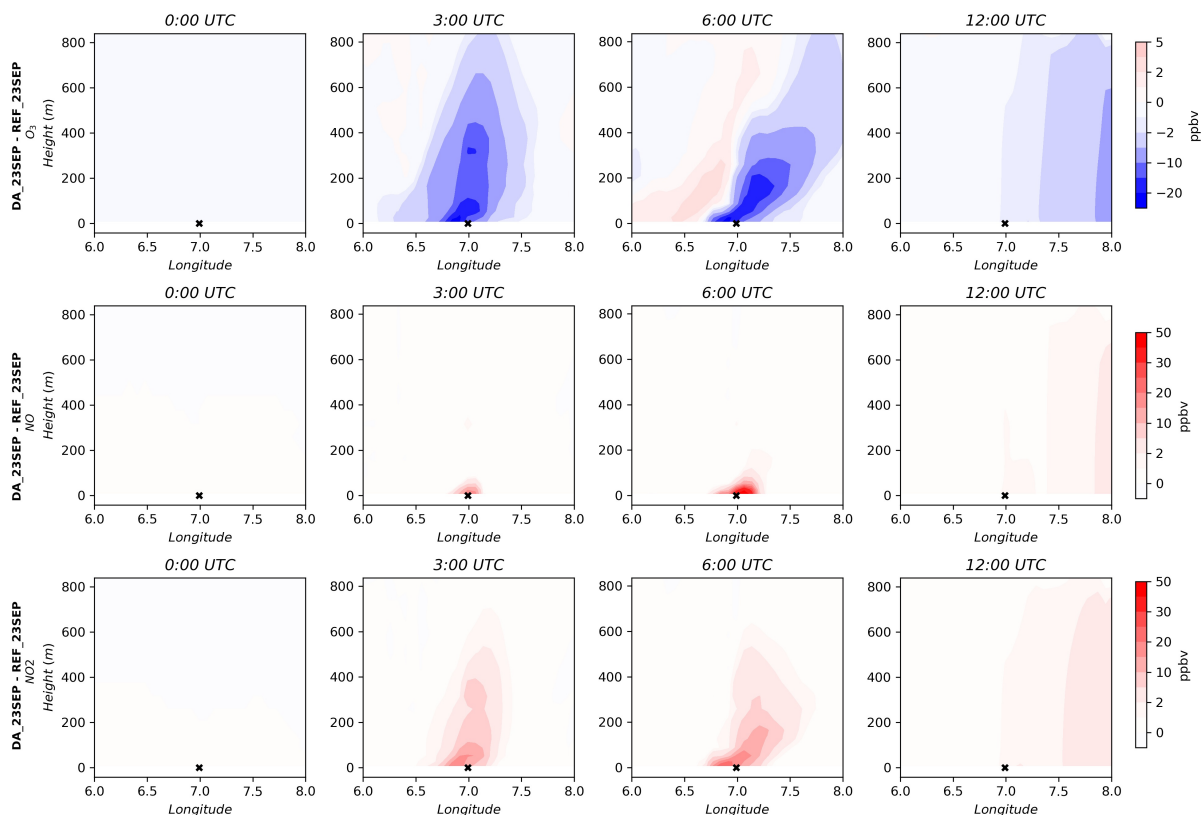
Figure 9. Vertical latitudinal cross-section of the analysis increment of O_3, NO and NO_2 on 23 September 2021 at selected time steps. The cross-section location is indicated by the dashed line between **A** and **B** in Fig. 8(e).

5 Discussion and conclusions

In this work, drone profile measurements of O_3 and NO are assimilated using the 4D-var data assimilation system of EURAD-IM. This represents the first application of drone data assimilation within a CTM. The primary objective is to assess the ability of drone observations to improve regional air quality analysis and to optimise emission rates when the joint initial value/emission correction factor optimisation approach is applied. The research is conducted using data collected during the two-day MesSBAR campaign in 2021. To evaluate the results, a comparison is made with ground-based observations taken at the same location as the assimilated data. Moreover, regional validation is conducted using ground-based data from the CAMS network. The 4D-var assimilation of drone data has a positive impact on the analysis. First, significant improvements are noted in the O_3 and NO vertical profiles, with biases decreasing by 30% and 55%, respectively, on the first day and by 35% on the second day for both species. Moreover, as expected, there is a noticeable impact on ground concentrations. In the studied grid cell, biases were lowered by up to 60% for O_3, 55% for NO, and 43% for NO_2 ground concentrations, all within the assimilation window. Furthermore, due to the pollution transport, a positive impact is seen on the ground concentrations of O_3 and NO_2 in locations farther from the measurement site during the assimilation window.

However, there were suboptimal outcomes observed in the free run, namely for O_3 and NO_2 ground concentration, suggesting that the advantage of the drone data assimilation is limited to the assimilation window (Fig.6, Fig.A4, and Fig.A5). Nevertheless, this result was not surprising and is completely explainable. Initially, it's important to note that the reference model simulation already provides underestimations of O_3 peaks during the afternoon and nighttime, which may be linked to uncertainties in the boundary layer height at night, vertical diffusion, and/or emissions. Through the 4D-var assimilation of drone data, adjustments were made to the NOx emissions. However, in regions characterised by high NOx emissions, ozone formation exhibited reduced sensitivity to NOx emissions but heightened sensitivity to VOCs (Visser et al., 2019; Sillman, 1999). Thus, the inability to adjust O_3 concentrations and, consequently, NO_2 in our simulations is not a limitation specific to drone data assimilation.

This study also identified the adjustment of emissions correction factors as a significant component in the reported analysis improvements, which underline the potential of the drone observations to be beneficial for emission optimisation. This finding aligns with the findings of Wu et al. (2022), affirming that observation at high altitudes can also be advantageous for optimising emissions under suitable wind conditions.

There are some limitations to this study. Firstly, due to constraints in data availability, the study is restricted to assimilating drone data within a singular grid cell column. Therefore, it would be advantageous to include multiple measurement points distributed across the region, strategically positioned both upwind and downwind of emission sources. As for the emission rate optimisation, the model considers a fixed diurnal emission profile, which causes uncertainties in the assimilation results. Another limitation of this study is the assimilation of data available only during a partial timeframe of the day. However, the inclusion of a more extensive observational dataset covering longer periods, ideally over 24 hours to enable an extended assimilation window, would greatly enhance the optimisation of emission rates.

In conclusion, the 4D-var assimilation of drone data within the regional air quality model EURAD-IM yields promising results

by improving the vertical distribution of pollutants and correcting ground concentrations. As a perspective for future work, one interesting approach is to conduct Observing System Experiments (OSE) to assess the advantages and limitations of integrating drone observations into CTMs through the application of a variational data assimilation technique.

Author contributions. HE and ACL designed the study. HE conducted the simulations, performed the analyses under scientific supervision of ACL, PF and AW. TS and RT provided the observational profile data. The manuscript was prepared by HE with the help of all co-authors. All authors reviewed the manuscript.

Competing interests. The authors declare that they have no conflict of interest.

Acknowledgements. The authors gratefully acknowledge all the MesSBAR project partners for their valuable efforts in conducting the campaign and processing the data used in this work. We also thank the Federal Highway Research Institute (BASt) for providing the ground-based observations and meteorological data. Financial support for the MesSBAR project was provided by the Modernity Fund mFUND of the Federal Ministry of Transport and Digital Infrastructure (BMVI) under grant agreement 19F2097. The authors also gratefully acknowledge the computing time granted through JARA on the supercomputer JURECA (Jülich Supercomputing Centre, 2021) at Forschungszentrum Jülich.

References

Ackermann, I. J., Hass, H., Memmesheimer, M., Ebel, A., Binkowski, F. S., and Shankar, U.: Modal aerosol dynamics model for Europe: development and first applications, Atmos. Environ., 32, 2981–2999, https://doi.org/10.1016/S1352-2310(98)00006-5, 1998.

390 Altstädter, B., Platis, A., Wehner, B., Scholtz, A., Wildmann, N., Hermann, M., Käthner, R., Baars, H., Bange, J., and Lampert, A.: ALADINA - an unmanned research aircraft for observing vertical and horizontal distributions of ultrafine particles within the atmospheric boundary layer, Atmos. Meas. Tech., 8, 1627–1639, https://doi.org/10.5194/amt-8-1627-2015, 2015.

Bretschneider, L., Schlerf, A., Baum, A., Bohlius, H., Buchholz, M., Düsing, S., Ebert, V., Erraji, H., Frost, P., Käthner, R., Krüger, T., Lange, A. C., Langner, M., Nowak, A., Pätzold, F., Rüdiger, J., Saturno, J., Scholz, H., Schuldt, T., Seldschopf, R., Sobotta, A., Tillmann, R.,

395 Wehner, B., Wesolek, C., Wolf, K., and Lampert, A.: MesSBAR-Multicopter and Instrumentation for Air Quality Research, Atmosphere, https://doi.org/10.3390/atmos13040629, 2022.

Corrigan, C. E., Roberts, G. C., Ramana, M. V., Kim, D., and Ramanathan, V.: Capturing vertical profiles of aerosols and black carbon over the Indian Ocean using autonomous unmanned aerial vehicles, Atmos. Chem. Phys., 8, 737–747, https://doi.org/10.5194/acp-8-737-2008, 2008.

400 Deroubaix, A., Hoelzemann, J. J., Ynoue, R. Y., de Almeida Albuquerque, T. T., Alves, R. C., de Fatima Andrade, M., ao, W. L. A., Bouarar, I., de Souza Fernandes Duarte, E., Elbern, H., Franke, P., Lange, A. C., Lichtig, P., Lugon, L., Martins, L. D., de Arruda Moreira, G., Pedruzzi, R., Rosario, N., and Brasseur, G.: Intercomparison of Air Quality Models in a Megacity: Toward an Operational Ensemble Forecasting System for São Paulo, J. Geophys. Res.: Atmospheres, 129, https://doi.org/10.1029/2022JD038179, 2024.

Diaz, J., Corrales, E., Madrigal, Y., Pieri, D., Bland, G., Miles, T., and Fladeland, M.: Volcano Monitoring with small Unmanned Aerial

405 Systems, American Institute of Aeronautics and Astronautics, https://doi.org/10.2514/6.2012-2522, 2012.

Duarte, E. D. S. F., Franke, P., Lange, A. C., Friese, E., da Silva Lopes, F. J., ao da Silva, J. J., dos Reis, J. S., Landulfo, E., e Silva, C. M. S., Elbern, H., and Hoelzemann, J. J.: Evaluation of atmospheric aerosols in the metropolitan area of São Paulo simulated by the regional EURAD-IM model on high-resolution, Atmos. Pollut. Res., 12, 451–469, https://doi.org/10.1016/j.apr.2020.12.006, 2021.

Elbern, H. and Schmidt, H.: Ozone episode analysis by four-dimensional variational chemistry data assimilation, J. Geophys. Res. Atmo-

410 spheres, 106, 3569–3590, https://doi.org/10.1029/2000JD900448, 2001.

Elbern, H., Strunk, A., Schmidt, H., and Talagrand, O.: Emission rate and chemical state estimation by 4-dimensional variational inversion, Atmos. Chem. Phys, 7, 3749–3769, https://doi.org/10.5194/acp-7-3749-2007, 2007.

Flagg, D. D., Doyle, J. D., Holt, T. R., Tyndall, D. P., Amerault, C. M., Geiszler, D., Haack, T., Moskaitis, J. R., Nachamkin, J., and Eleuterio, D. P.: On the Impact of Unmanned Aerial System Observations on Numerical Weather Prediction in the Coastal Zone, Mon. Wea. Rev.,

415 146, 599–622, https://doi.org/10.1175/MWR-D-17-0028.1, 2018.

Franke, P., Lange, A. C., and Elbern, H.: Particle-filter-based volcanic ash emission inversion applied to a hypothetical sub-Plinian Eyjaf-jallajökull eruption using the Ensemble for Stochastic Integration of Atmospheric Simulations (ESIAS-chem) version 1.0, Geosci. Model Dev., 15, 1037–1060, https://doi.org/10.5194/gmd-15-1037-2022, 2022.

Gama, C., Ribeiro, I., Lange, A. C., Vogel, A., Ascenso, A., Seixas, V., Elbern, H., Borrego, C., Friese, E., and Monteiro, A.: Performance

420 assessment of CHIMERE and EURAD-IM' dust modules, Atmos. Pollut. Res., 10, 1336–1346, https://doi.org/10.1016/j.apr.2019.03.005, 2019.

Guenther, A. B., Jiang, X., Heald, C. L., Sakulyanontvittaya, T., Duhl, T., Emmons, L. K., and Wang, X.: The Model of Emissions of Gases and Aerosols from Nature version 2.1 (MEGAN2.1): an extended and updated framework for modeling biogenic emissions, Geosci. Model Dev., 5, 1471–1492, https://doi.org/10.5194/gmd-5-1471-2012, 2012.

425 Illingworth, S., Allen, G., Percival, C., Hollingsworth, P., Gallagher, M., Ricketts, H., Hayes, H., ÅĄadosz, P., Crawley, D., and Roberts, G.: Measurement of boundary layer ozone concentrations on-board a Skywalker unmanned aerial vehicle, Atmos. Sci. Lett., 15, 252–258, https://doi.org/10.1002/asl2.496, 2014.

Jensen, A. A., Pinto, J. O., Bailey, S. C. C., Sobash, R. A., de Boer, G., Houston, A. L., Chilson, P. B., Bell, T., Romine, G., Smith, S. W., Lawrence, D. A., Dixon, C., Lundquist, J. K., Jacob, J. D., Elston, J., Waugh, S., and Steiner, M.: Assimilation of a Coordinated Fleet of

430 Uncrewed Aircraft System Observations in Complex Terrain: EnKF System Design and Preliminary Assessment, Mon. Wea. Rev., 149, 1459–1480, https://doi.org/10.1175/MWR-D-20-0359.1, 2021.

Jonassen, M. O., Ólafsson, H., Ágústsson, H., Ólafur Rögnvaldsson, and Reuder, J.: Improving High-Resolution Numerical Weather Simulations by Assimilating Data from an Unmanned Aerial System, Mon. Wea. Rev., 140, 3734–3756, https://doi.org/10.1175/MWR-D-11-00344.1, 2012.

435 Jülich Supercomputing Centre: JURECA: Data Centric and Booster Modules implementing the Modular Supercomputing Architecture at Jülich Supercomputing Centre, Journal of large-scale research facilities JLSRF, 7, A182, https://doi.org/10.17815/jlsrf-7-182, 2021.

Klonecki, A., Pommier, M., Clerbaux, C., Ancellet, G., Cammas, J.-P., Coheur, P.-F., Cozic, A., Diskin, G. S., Hadji-Lazaro, J., Hauglustaine, D. A., Hurtmans, D., Khattatov, B., Lamarque, J.-F., Law, K. S., Nedelec, P., Paris, J.-D., Podolske, J. R., Prunet, P., Schlager, H., Szopa, S., and Turquety, S.: Assimilation of IASI satellite CO fields into a global chemistry transport model for validation against aircraft

440 measurements, Atmos. Chem. Phys., 12, 4493–4512, https://doi.org/10.5194/acp-12-4493-2012, 2012.

Kuenen, J. J. P., Visschedijk, A. J. H., Jozwicka, M., and van der Gon, H. A. C. D.: TNO-MACC-II emission inventory; a multi-year (2003-2009) consistent high-resolution European emission inventory for air quality modelling, Atmos. Chem. Phys., 14, 10 963–10 976, https://doi.org/10.5194/acp-14-10963-2014, 2014.

Lampert, A., Altstädter, B., Bärfuss, K., Bretschneider, L., Sandgaard, J., Michaelis, J., Lobitz, L., Asmussen, M., Damm, E., Käthner, R.,

445 Krüger, T., Lüpkes, C., Nowak, S., Peuker, A., Rausch, T., Reiser, F., Scholtz, A., Zakharov, D. S., Gaus, D., Bansmer, S., Wehner, B., and Pätzold, F.: Unmanned Aerial Systems for Investigating the Polar Atmospheric Boundary Layer - Technical Challenges and Examples of Applications, Atmosphere, 11, 416, https://doi.org/10.3390/atmos11040416, 2020.

Lawrence, D. A. and Balsley, B. B.: High-Resolution Atmospheric Sensing of Multiple Atmospheric Variables Using the DataHawk Small Airborne Measurement System, J. Atmos. Ocean. Technol., 30, 2352–2366, https://doi.org/10.1175/JTECH-D-12-00089.1, 2013.

450 Leuenberger, D., Haefele, A., Omanovic, N., Fengler, M., Martucci, G., Calpini, B., Fuhrer, O., and Rossa, A.: Improving High-Impact Numerical Weather Prediction with Lidar and Drone Observations, Bull. Am. Meteorol. Soc., 101, E1036–E1051, https://doi.org/10.1175/BAMS-D-19-0119.1, 2020.

Liu, D. C. and Nocedal, J.: On the limited memory BFGS method for large scale optimization, Math. Program., 45, 503–528, https://doi.org/10.1007/BF01589116, 1989.

455 Liu, X., Mizzi, A. P., Anderson, J. L., Fung, I. Y., and Cohen, R. C.: Assimilation of satellite NO2 observations at high spatial resolution using OSSEs, Atmos. Chem. Phys., 17, 7067–7081, https://doi.org/10.5194/acp-17-7067-2017, 2017.

Maréchal, V., Peuch, V.-H., Andersson, C., Andersson, S., Arteta, J., Beekmann, M., Benedictow, A., Bergström, R., Bessagnet, B., Cansado, A., Chéroux, F., Colette, A., Coman, A., Curier, R. L., Denier van der Gon, H. A. C., Drouin, A., Elbern, H., Emili, E., Engelen, R. J., Eskes, H. J., Foret, G., Friese, E., Gauss, M., Giannaros, C., Guth, J., Joly, M., Jaumouillé, E., Josse, B., Kadygrov, N., Kaiser, J. W., Kra-

460   jsek, K., Kuenen, J., Kumar, U., Liora, N., Lopez, E., Malherbe, L., Martinez, I., Melas, D., Meleux, F., Menut, L., Moinat, P., Morales, T., Parmentier, J., Piacentini, A., Plu, M., Poupkou, A., Queguiner, S., Robertson, L., Rouïl, L., Schaap, M., Segers, A., Sofiev, M., Tarasson, L., Thomas, M., Timmermans, R., Valdebenito, A., van Velthoven, P., van Versendaal, R., Vira, J., and Ung, A.: A regional air quality forecasting system over Europe: the MACC-II daily ensemble production, Geosci. Model Dev., 8, 2777–2813, https://doi.org/10.5194/gmd-8-2777-2015, 2015.

465   Martin, R. V.: Satellite remote sensing of surface air quality, Atmos. Environ., 42, 7823–7843, https://doi.org/10.1016/j.atmosenv.2008.07.018, 2008.

Memmesheimer, M., H. Hass, J. Tippke, and A. Ebel: Modeling of episodic emission data for Europe with the EURAD Emission Model EEM, in: the International Speciality Conference "Regional Photochemical Measurement and modeling studies", San Diego, CA, USA, 1995.

470   Nathan, B. J., Golston, L. M., O'Brien, A. S., Ross, K., Harrison, W. A., Tao, L., Lary, D. J., Johnson, D. R., Covington, A. N., Clark, N. N., and Zondlo, M. A.: Near-Field Characterization of Methane Emission Variability from a Compressor Station Using a Model Aircraft, Environ. Sci. Technol., 49, 7896–7903, https://doi.org/10.1021/acs.est.5b00705, 2015.

O'Sullivan, D., Taylor, S., Elston, J., Baker, C. B., Hotz, D., Marshall, C., Jacob, J., Barfuss, K., Piguet, B., Roberts, G., Omanovic, N., Fengler, M., Jensen, A. A., Steiner, M., and Houston, A. L.: The Status and Future of Small Uncrewed Aircraft Systems (UAS) in
475   Operational Meteorology, Bull. Am. Meteorol. Soc., 102, E2121–E2136, https://doi.org/10.1175/BAMS-D-20-0138.1, 2021.

Paschalidi, Z.: Inverse Modelling for Tropospheric Chemical State Estimation by 4-Dimensional Variational Data Assimilation from Routinely and Campaign Platforms, Ph.D. thesis, University of Cologne, 2015.

Petetin, H., Jeoffrion, M., Sauvage, B., Athier, G., Blot, R., Boulanger, D., Clark, H., Cousin, J.-M., Gheusi, F., Nedelec, P., Steinbacher, M., and Thouret, V.: Representativeness of the IAGOS airborne measurements in the lower troposphere, Elementa-Sci. Anthrop., 6,
480   https://doi.org/10.1525/elementa.280, 2018.

Rabitz, H. and Aliş, O. F.: General foundations of high-dimensional model representations, J. Math. Chem., 25, 197–233, https://doi.org/10.1023/A:1019188517934, 1999.

Roberts, G. C., Ramana, M. V., Corrigan, C., Kim, D., and Ramanathan, V.: Simultaneous observations of aerosol-cloud-albedo interactions with three stacked unmanned aerial vehicles, P. Natl. Acad. Sci. USA, 105, 7370–7375, https://doi.org/10.1073/pnas.0710308105, 2008.

485   Roselle, S. and Binkowski, F.: Cloud Dynamics and Chemistry, in Science Algorithms of the EPA Models-3 Community Multiscale Air Quality (CMAQ) Modeling System, Research Triangle Park, EPA 600/R-99-030, 1999.

Sandu, A. and Sander, R.: Technical note: Simulating chemical systems in Fortran90 and Matlab with the Kinetic PreProcessor KPP-2.1, Atmos. Chem. Phys, 6, 187–195, https://doi.org/10.5194/acp-6-187-2006, 2006.

Scheffe, R., Philbrick, R., on Macdonald, C., Dye, T., Gilroy, M., and Carlton, A.-M.: Observational Needs for Four-dimensional Air Quality
490   Characterization, https://cfpub.epa.gov/si/si_public_record_report.cfm?Lab=NERL&dirEntryId=213564, 2009.

Schell, B., Ackermann, I. J., Hass, H., Binkowski, F. S., and Ebel, A.: Modeling the formation of secondary organic aerosol within a comprehensive air quality model system, J. Geophys. Res.: Atmospheres, 106, 28 275–28 293, https://doi.org/10.1029/2001JD000384, 2001.

Schuldt, T., Gkatzelis, G. I., Wesolek, C., Rohrer, F., Winter, B., Kuhlbusch, T. A. J., Kiendler-Scharr, A., and Tillmann, R.: Electro-
495   chemical sensors on board a Zeppelin NT: in-flight evaluation of low-cost trace gas measurements, Atmos. Meas. Tech., 16, 373–386, https://doi.org/10.5194/amt-16-373-2023, 2023.

Schuyler, T. and Guzman, M.: Unmanned Aerial Systems for Monitoring Trace Tropospheric Gases, Atmosphere, 8, 206, https://doi.org/10.3390/atmos8100206, 2017.

Sillman, S.: The relation between ozone, NOx and hydrocarbons in urban and polluted rural environments, Atmos. Environ., 33, 1821–1845,
500   https://doi.org/10.1016/S1352-2310(98)00345-8, 1999.

Skamarock, W. C., Klemp, J. B., Dudhia, J., Gill, D. O., Barker, D. M., Duda, M. G., Huang, X.-Y., Wang, W., and Powers, J. G.: A Description of the Advanced Research WRF Version 3, 2008.

Stockwell, W. R., Kirchner, F., Kuhn, M., and Seefeld, S.: A new mechanism for regional atmospheric chemistry modeling, J. Geophys. Res., 102, 847–872, https://doi.org/10.1029/97JD00849, 1997.

505   Sun, Q., Vihma, T., Jonassen, M. O., and Zhang, Z.: Impact of Assimilation of Radiosonde and UAV Observations from the Southern Ocean in the Polar WRF Model, Adv. Atmos. Sci., 37, 441–454, https://doi.org/10.1007/s00376-020-9213-8, 2020.

Tillmann, R., Gkatzelis, G. I., Rohrer, F., Winter, B., Wesolek, C., Schuldt, T., Lange, A. C., Franke, P., Friese, E., Decker, M., Wegener, R., Hundt, M., Aseev, O., and Kiendler-Scharr, A.: Air quality observations onboard commercial and targeted Zeppelin flights in Germany - a platform for high-resolution trace-gas and aerosol measurements within the planetary boundary layer, Atmos. Meas. Tech., 15, 3827–3842,
510   https://doi.org/10.5194/amt-15-3827-2022, 2022.

Villa, T., Gonzalez, F., Miljievic, B., Ristovski, Z., and Morawska, L.: An Overview of Small Unmanned Aerial Vehicles for Air Quality Measurements: Present Applications and Future Prospectives, Sensors, 16, 1072, https://doi.org/10.3390/s16071072, 2016.

Visser, A. J., Boersma, K. F., Ganzeveld, L. N., and Krol, M. C.: European NO_x emissions in WRF-Chem derived from OMI: impacts on summertime surface ozone, Atmos. Chem. Phys., 19, 11 821–11 841, https://doi.org/10.5194/acp-19-11821-2019, 2019.

515   Walcek, C. J.: Minor flux adjustment near mixing ratio extremes for simplified yet highly accurate monotonic calculation of tracer advection, J. Geophys. Res.: Atmospheres, 105, 9335–9348, https://doi.org/10.1029/1999JD901142, 2000.

Wang, H., Lu, X., Jacob, D. J., Cooper, O. R., Chang, K.-L., Li, K., Gao, M., Liu, Y., Sheng, B., Wu, K., Wu, T., Zhang, J., Sauvage, B., Nédélec, P., Blot, R., and Fan, S.: Global tropospheric ozone trends, attributions, and radiative impacts in 1995-2017: an integrated analysis using aircraft (IAGOS) observations, ozonesonde, and multi-decadal chemical model simulations, Atmos. Chem. Phys., 22,
520   13 753–13 782, https://doi.org/10.5194/acp-22-13753-2022, 2022.

Wang, Y.-C., Wang, S.-H., Lewis, J. R., Chang, S.-C., and Griffith, S. M.: Determining Planetary Boundary Layer Height by Micro-pulse Lidar with Validation by UAV Measurements, Aerosol. Air. Qual. Res., 21, 200 336, https://doi.org/10.4209/aaqr.200336, 2021.

Weaver, A. and Courtier, P.: Correlation modelling on the sphere using a generalized diffusion equation, Q. J. Roy. Meteor. Soc., 127, 1815–1846, https://doi.org/https://doi.org/10.1002/qj.49712757518, 2001.

525   Wu, X., Elbern, H., and Jacob, B.: The assessment of potential observability for joint chemical states and emissions in atmospheric modelings, Stoch. Environ. Res. Risk. Assess., 36, 1743–1760, https://doi.org/10.1007/s00477-021-02113-x, 2022.

Yang, S., Li, X., Zeng, L., Yu, X., Liu, Y., Lu, S., Huang, X., Zhang, D., Xu, H., Lin, S., Liu, H., Feng, M., Song, D., Tan, Q., Cui, J., Wang, L., Chen, Y., Wang, W., Sun, H., Song, M., Kong, L., Liu, Y., Wei, L., Zhu, X., and Zhang, Y.: Development of multi-channel whole-air sampling equipment onboard an unmanned aerial vehicle for investigating volatile organic compounds' vertical distribution in
530   the planetary boundary layer, Atmos. Meas. Tech., 16, 501–512, https://doi.org/10.5194/amt-16-501-2023, 2023.

Zhang, L., Brook, J. R., and Vet, R.: A revised parameterization for gaseous dry deposition in air-quality models, Atmos. Chem. Phys., 3, 2067–2082, https://doi.org/10.5194/acp-3-2067-2003, 2003.

Appendix A

Table A1. Information about the Ground-based monitoring stations.

Station Number	Station Code	Station Name	Distance from the compaign site	Station Type	Latitude(°N)	Longitude (°E)	Altitude
8	DENW008	Dortmund-Eving	86.5 km	Suburban	51.5369	7.4575	75 m
53	DENW053	Köln-Chorweiler	28.2 km	Suburban	51.0193	6.8846	45 m
59	DENW059	Köln-Rodenkirchen	12.1 km	Rural	50.8898	6.9852	45 m
80	DENW080	Solingen-Wald	43.2 km	Rural	51.1838	7.0526	207 m
114	DENW114	Wuppertal-Langerfeld	56.8 km	Suburban	51.2776	7.2319	186 m
179	DENW179	Schwerte	82.4 km	Suburban	51.4488	7.5823	157 m
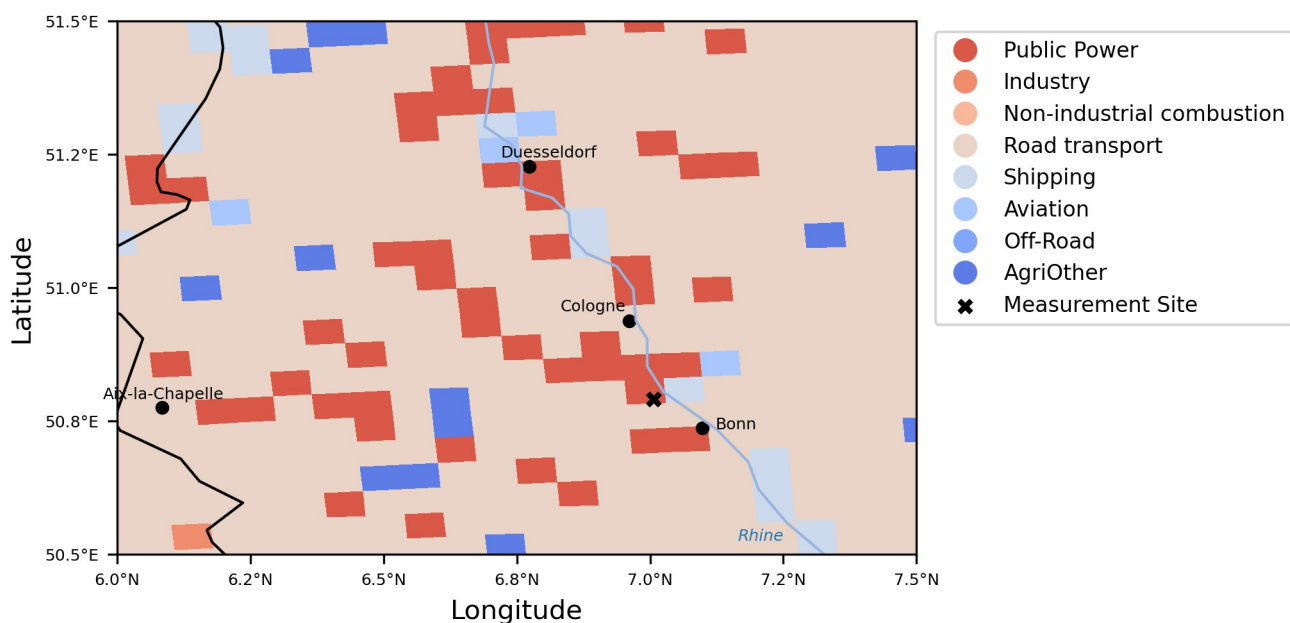
Figure A1. The dominant sector of NOx emissions within each model grid cell for the region around the MesSBAR campaign site.
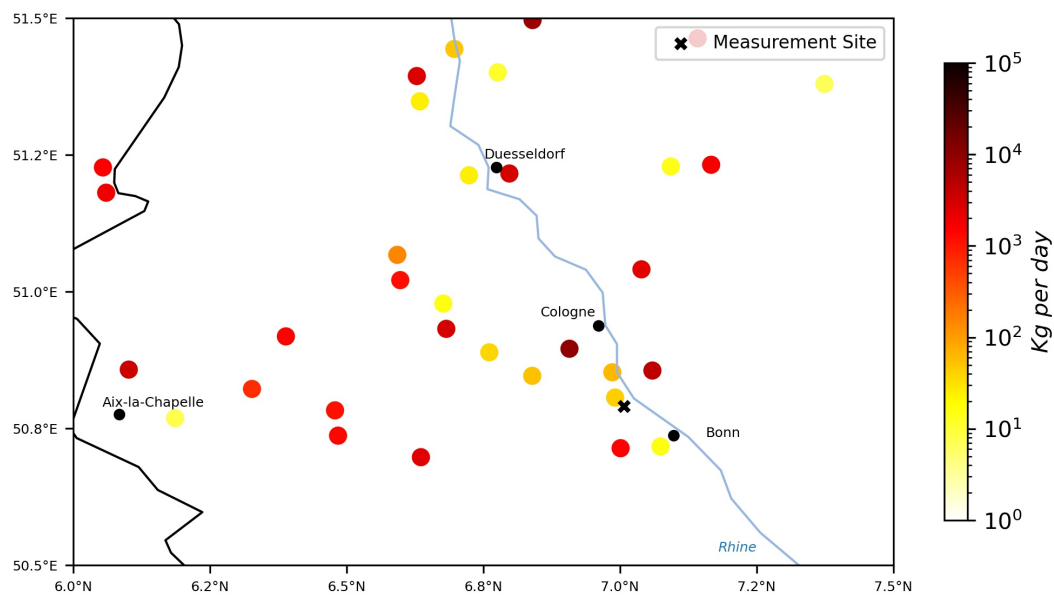
Figure A2. NOx emission point sources in the region around the MesSBAR campaign location
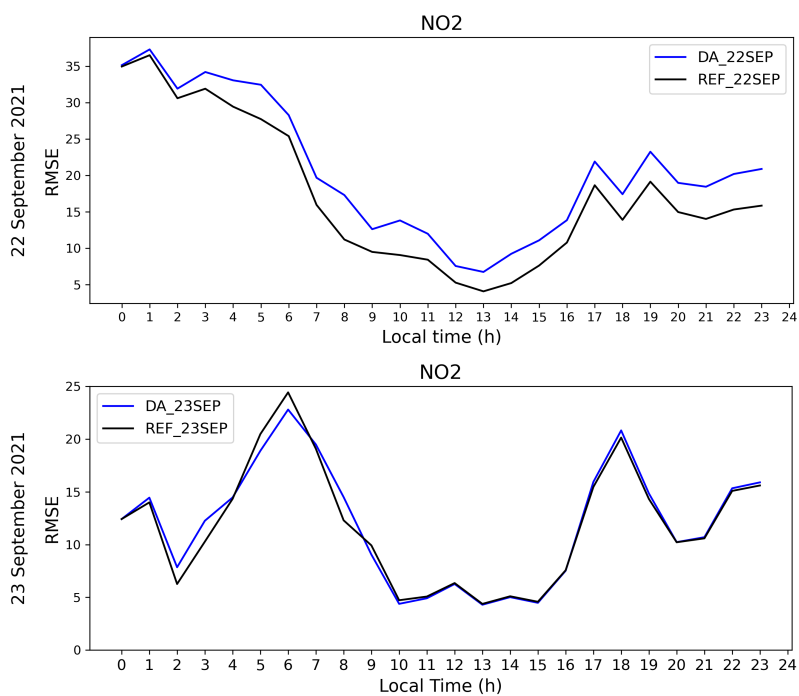
Figure A3. Temporal evolution of the RMSE (model-observations) in ppbv for NO_2 calculated for the background (black) and the analysis (blue) over the 24-hour forecast period across all ground stations on 22 September 2021 (top) and 23 September 2021 (bottom).
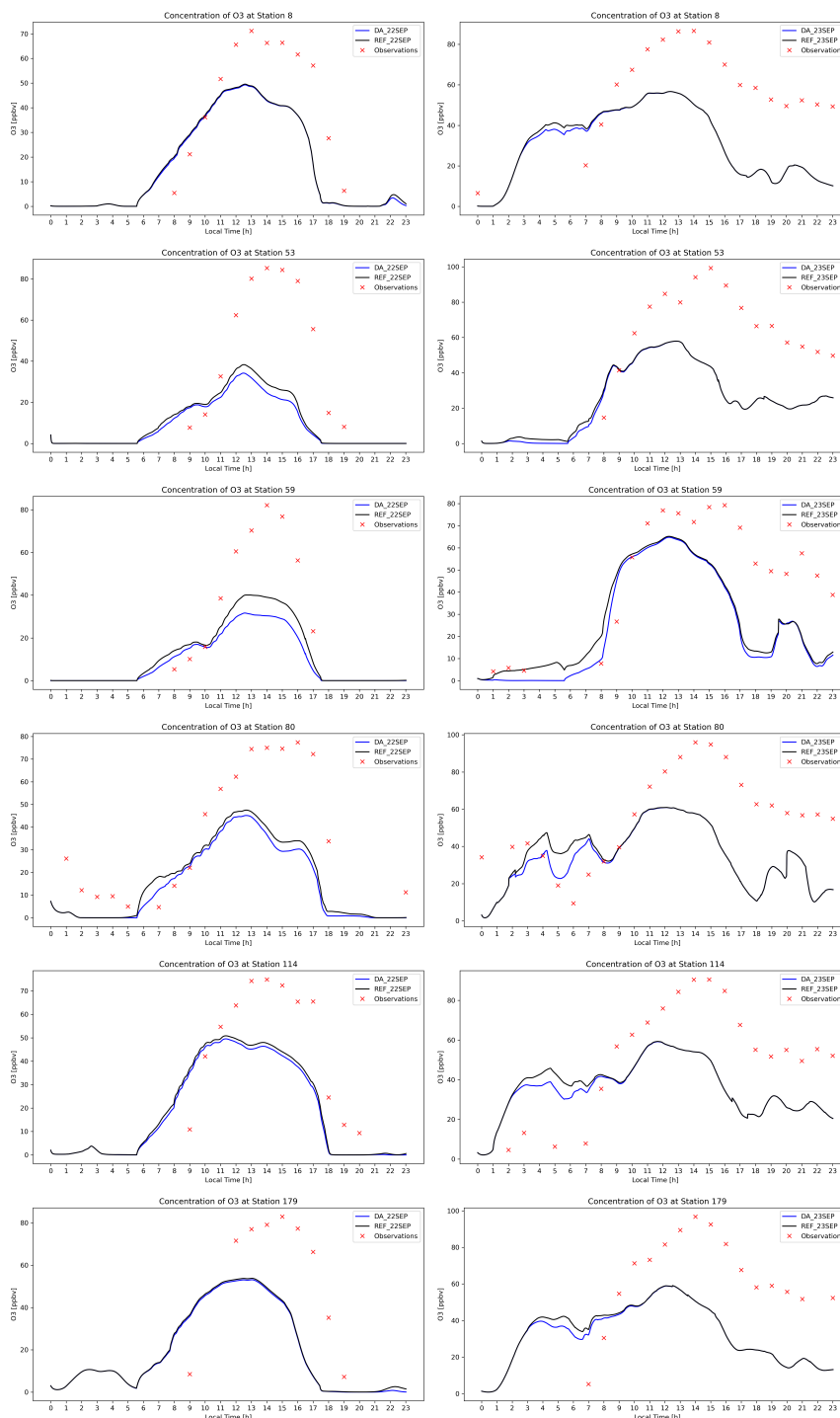
Figure A4. Time series of O$_3$ concentrations in ppb as measured by ground-based stations and predicted by the model. The left panel shows data from September 21, 2021, while the right panel displays data from September 23, 2021.
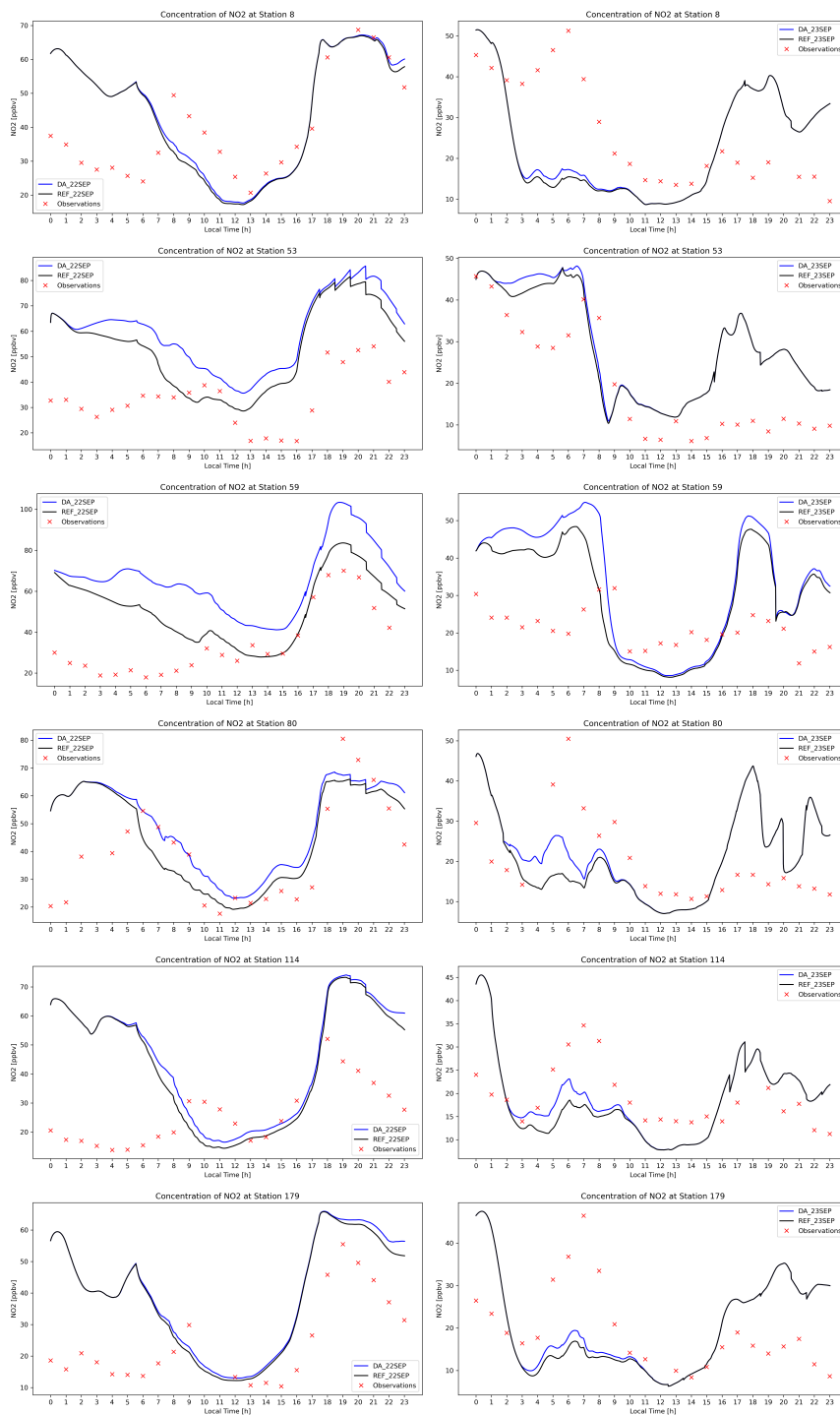
Figure A5. Same as Figure A4 but for NO$_2$.